ELSEVIER

Journal of Volcanology and Geothermal Research 102 (2000) 339–361

Journal of volcanology and geothermal research

www.elsevier.nl/locate/jvolgeores

Genetic links between ash-flow calderas and associated ore deposits as revealed by large-scale thermo-mechanical modeling

L. Guillou-Frottier*, E.B. Burov[1], J.-P. Milési

BRGM, REM/MESY, 3 av. C. Guillemin, BP6009, 45060 Orleans Cedex 2, France

Received 25 October 1999; revised 7 June 2000; accepted 7 June 2000

Abstract

In addition to a number of epithermal ore deposits, some porphyry-type ore deposits are also hosted by ash-flow calderas. Spatial correlation between ash-flow calderas and these deposits is observed in several parts of the world, but temporal correlation between the mineralization and the episode of caldera formation remains unclear, especially because geochronological data indicate that the mineralization may date to several million years before or after caldera formation. Because caldera collapse represents only a very short event in a long time-scale evolution between a silicic magma chamber and its host rocks, we have developed a thermo-mechanical model of upper crustal and magmatic system behavior during the pre- and post-caldera formation stages. Major petrophysical properties of ash-flow caldera related rocks are incorporated into the model, which accounts for brittle–elasto-ductile rheology and heat transfer, and reproduces fault initiation and various caldera collapse scenarios. Large-scale mechanisms of initiation of thermal and structural traps for epithermal ore deposits are described. In particular, we found that the outer sides of caldera border faults are associated with both anomalous heat-transfer and a high fracture density. The finite size of the insulating intracaldera units forces the accumulated heat excess to be laterally transferred across the border faults. In most cases, the model predicts "Y-shaped" fault geometry, which is surprisingly similar to that of mineralized faults in the field. Variations in lithostatic pressure on the magma chamber roof and in the vicinity of the border faults can reach 10 to 20 MPa, with deep overpressured zones close to the inner edge of the chamber corners. Despite the fact that hydrothermal convection and fluid geochemistry are not included in the model, these thermal and mechanical results are believed to constrain the conditions for mineralization processes. Our results show that in the presence of regional extension, the development of caldera border faults may be suppressed to the advantage of deep-seated fractures, clustered above the central part of the magma chamber, thus favoring conditions for the formation of porphyry-type ore deposits. Finally, we demonstrate that well before the eruption, the gradual emplacement of a hot and large silicic magma chamber may create significant extensional stress in the brittle upper crust, resulting in breakup and pre-eruptive normal faulting and thus allowing for conditions of pre-caldera mineralization.

Keywords: ash-flow tuff; caldera collapse; faulting; ore deposits; thermo-mechanical processes; modeling

1. Introduction

Epithermal ore deposits are commonly associated with fractured and faulted zones in the upper crust, where circulating hydrothermal fluids exchange heat and matter with the host rocks allowing mineralization processes to take place. These fluids, enriched

* Corresponding author. Tel.: +33-2-38-64-47-91; fax: +33-2-38-64-36-52.

E-mail addresses: l.guillou-frottier@brgm.fr (L. Guillou-Frottier), evgenii.burov@lgs.jussieu.fr (E.B. Burov), jp.milesi@brgm.fr (J.-P. Milési).

[1] Laboratoire de Tectonique ESA7072, T26-E1, case 129, Université Pierre et Marie Curie, 4 Place Jussieu, 75252 Paris Cedex 05, France.

0377-0273/00/$ - see front matter
PII: S0377-0273(00)00246-8

with metals from an underlying magma chamber, are absorbed by the meteoric water participating in the hydrothermal circulation (Hedenquist and Lowenstern, 1994). Field observations indicate that a large number of epithermal ore deposits are spatially related to ash-flow caldera settings (e.g. White and Hedenquist, 1990; Lipman, 1992; Rytuba, 1994; Milési et al., 1999).

The existence of a genetic link between caldera systems and ore deposits is not, however, fully accepted because of a number of mis-correlations in the time domain, with caldera formation being separated from the mineralization stages by as much as several million years (see examples in Table 1). Contrary to the statistically close relationship between caldera settings and ore deposits, this observation may raise doubts concerning the existence of a genetic link (McKee, 1979). Several examples of temporal misfits spanning a few million years between mineralization stages and caldera collapse can be quoted: the Cerro La Joya district (Redwood, 1987) was formed about 10 m.y. before development of the neighboring Soledad caldera; south of the Valles caldera, New Mexico, the Cochiti gold district is dated as being about 5 m.y. older than caldera collapse at 1.13 Ma (Goff and Gardner, 1994). In the case of the Lake City caldera in Colorado, major ore-bearing veins were emplaced within the forming caldera during resurgent doming and granitic intrusion, but minor quartz-pyrite veins also appeared 2 m.y. before caldera collapse (Slack, 1980, and other examples in Table 1). In general, mineralization stages partially coincide with caldera formation and subsequent subsidence, as for the epithermal deposits in the Toquima caldera complex, Nevada (Sander and Einaudi, 1990), although regional faults are also known to reactivate adjacent caldera border faults, thus leading to "post-mineralization" independent of the dynamic behavior of the caldera (e.g. tectonic control in the Pongkor area, Milési et al., 1999). Despite certain mineralization phases being coeval with caldera collapse, a genetic link between ore deposits and neighboring calderas is not yet well established. It should be noted that the overall evolution of the "caldera-host rock" system has not usually been taken into sufficient consideration during the study of mineralization timing.

The first objective of this study is to demonstrate how and why favorable traps for minerals and ore deposits can be created in ash-flow caldera settings. We present some thermal and mechanical processes that lead to enhanced "trapping" capabilities of the outer sides of the border faults. The presence and location of major faults (such as border faults) are shown to be strongly dependent on magma chamber geometry, in addition to being controlled by the regional stress regime. The geometry of major faults appears to be more sensitive to temperature-dependent rheology. Depending on the evolution of the extensional stress regime, ore deposits can switch from being epithermal type to porphyry type. Our results also describe how conjugate faults joining at depth ("Y-shaped" faults) are created at caldera borders. The second objective deals with temporal relationships: we show that the border faults of ash-flow calderas can be initiated long before eruption (and thus before caldera collapse) by certain thermo-mechanical processes that may occur during magma reservoir settlement within the shallow crust. Hence, mineralization that precedes caldera formation may in fact be compatible with the "genetic link" concept, implying that simple geochronological data alone are not sufficient to discriminate whether ore deposit formation and caldera collapse are closely related or not. Our calculations also show that long-term or quasi steady-state anomalous stress/pressure variations and heat transfer processes need to be considered during a study of mineralization timing.

Although our interpretations are constrained by several field examples, the reader should bear in mind that mineralization cannot be modeled without taking into account both thermal and mechanical processes (this study) and also hydrodynamic and chemical interactions between the hot mineralized fluids and their fractured host rocks. Unfortunately, the formation of thermal and structural traps for ore deposits has not been sufficiently studied and understood yet, to support the creation of a complete four-fold coupled model. For example, fluid circulation can be largely controlled by poorly constrained permeability variations in the fractured host matrix. On the other hand, some authors claim that the presence of strong (e.g. fault induced) pressure gradients can completely overprint and dilute the effect of the permeable matrix on the fluid pathways (Y. Podladchikov, personal communication).

2. Mineralization within caldera settings

Once formed, ash-flow (or ignimbrite) calderas can clearly provide favorable conditions for mineralization: the underlying silicic magma chamber may be sufficiently hot to maintain a strong circulation of hydrothermal fluids within the permeable ash-flow units. Intracaldera rocks have very different physical properties from those of adjacent units (see Section 3), some of which are able to favor particular fluid–rock interactions. For example, because intracaldera rocks are highly porous at the surface, meteoric water commonly becomes involved in the whole convecting system (Criss et al., 1991), leading to an efficient mixing of fluids from different sources. Moreover, caldera border faults and fractures provide the possibility of vertical hydrothermal flow.

Despite such favorable geological features, ash-flow calderas are not necessarily mineralized. In some cases, neighboring calderas, apparently formed under similar conditions appear either barren or mineralized, such as the Los Frailes and Rodalquilar-Lomilla calderas in southeastern Spain, (Rytuba et al., 1990; Cunningham et al., 1990). In addition, when the regional tectonic regime changes in a volcanic area, caldera-related ore deposits can evolve from the epithermal type to the porphyry type, as demonstrated in the Philippines before the Late Miocene (Mitchell and Balce, 1990). It is not uncommon to find both epithermal- and porphyry-type ore deposits only a few kilometers apart, especially in areas having undergone regional extension, significant erosion or volcanism (see the example in Fig. 1 adapted from Semple et al. (1998), where a graben coexists with two circular structures, each being differently mineralized). In Romania, different types of ore deposits in clusters are well documented by Mitchell (1996). Another case, probably due to strong erosion and subsequent uplift, is observed in the Minas Conga district, Peru, where high-sulfidation epithermal ore deposits and porphyry-copper deposits lie only a few kilometers apart around a large ($\approx 20 \times 20\ km^2$) volcano-tectonic depression (Llosa et al., 1996). Hence, regional tectonics might play a major role in the emplacement processes and the type of mineralization associated with caldera settings.

In order to illuminate the mineralization potential of ash-flow calderas, we adopted an approach aimed at understanding large-scale thermo-mechanical processes responsible for initiating thermal and structural traps for ore deposits. To achieve this, we took into consideration “caldera-scale” factors (i.e. the “host rock-fault-ignimbrite” system together with the magma chamber) as well as external parameters such as the regional stress field and thermal regimes of the crust. Inherently, we assumed in this study that ore deposit formation is favored in areas where fracture density is the highest and where particular heat and mass exchanges are likely to take place. Hydrothermal convection and fluid geochemistry were not included although we accept that mineralization processes cannot be studied in detail without considering a fully coupled model (thermal, mechanical, hydrodynamical and chemical).

3. Thermo-mechanical processes in ash-flow calderas

Calderas associated with explosive ash-flow eruptions have been studied for several decades (e.g. Williams, 1941; Smith and Bailey, 1968; Lipman, 1997) and the formation scenario of ash-flow calderas by some form of roof collapse is now well accepted. Different source mechanisms for caldera collapse are nevertheless plausible: external overload (ash-flow units) breaking the cover from above, overpressure within the magma chamber initiating fractures in the cover from below, or some kind of suction effect following eruption (Roche et al., 2000). Whatever the invoked mechanism, the number and probable location of weak zones within ash-flow calderas has only been studied using rather simplified rheological laws and hypotheses on magma chamber geometry (Marti et al., 1994; De Natale et al., 1997; Gudmunsson, 1998). In these and similar recent studies, fault localization has not been resolved, and the thermal effects on the rheological behavior of caldera-related rocks have not been included (see however Chéry et al., 1991, where magma reservoir geometry remains fixed). In our numerical simulations of caldera formation and evolution presented below, stress distribution and fault initiation are resolved, and temperature-dependent rheology as well as the petrophysical properties of ash-flow caldera-related rocks are taken into

Table 1
Examples of mineralized ash-flow calderas

Country/state	Caldera/deposit	Age of caldera (Ma)	Diameter (km)	d[a] (km)	Chronology of magmatic events	Mineralization	Ages (Ma) of mineralization	Pre/Syn or post- caldera mineralization	Ref.
Low sulfidation epithermal ore deposits									
BOLIVIA	Soledad/La Joya	5.4	22 × 14	0.13	15 Ma: dacitic intrusions and mineralization 8.8 Ma: rhyolitic domes along ring fracture 5.4 Ma: caldera collapse and Soledad Tuffs	Au–Ag–Cu–Pb–Zn	15	Pre	Redwood (1987)
	Porco	12	5 × 3	0.4	12 Ma: Porco Tuff; 9–6 Ma: Los Frailes 8.6 Ma: centered Huayana Porco Stocks 8.6 Ma: ring dykes with mineralization	Ag–Zn–Pb–Sn	8.6	Post	Cunningham et al. (1994)
FIJI	Tavua/Emperor	4.0–5.0	7 × 6	0.8–1.8	5 Ma: extrusion of shoshonitic volcanics; subsidence and formation of an inner caldera, “Turtle” then “Morrisson” Pool formations	Au–Ag–Te	unknown: up to 8 stages during waning stages of the Morrisson volcanism		Anderson and Eaton (1990); Ahmad and Walshe (1990)
INDONESIA	Pongkor	5.7–2.05	8 × 6	0.3	15.3–9.4 Ma: intermittent volcanism 5.7–2.0 Ma: major volcano-magmatic episode including ignimbritic caldera cross-cut by mineralized veins	Au–Ag	2.05	Post	Marcoux et al. (1996); Milési et al. (1999)
	Citorek/Cirotan	3.6	60		9.5 Ma: rhyodacite ignimbrite; then older dacitic and andesitic intrusions 4.5–Ma: late stock of microdiorite. Mineralization hosted by later fractures	Au–Ag–(Mn)	1.7	Post	Milési et al. (1994)
JAPAN	Takatama	9	15	0.8	9 Ma: caldera formation, resurgent rhyolitic dome 7.8 Ma: mineralization; 7.5 Ma: andesite eruption	Au–Ag	7.8	Post	Seki (1993);
PERU	Cerro Sagollan/ Nevado Portugueza	2.4	7 × 4	0.8	2.4 Ma: explosive volcanism: Atunsulla Tuff 1.9 Ma: rhyodacite dome, slight resurgence and mineralization; hydrothermal activity before and after 2.4 Ma	Ag–Au	1.9	Post	Noble and McKee (1982)
	Julcani	10	7.5 × 6.5		Dacitic and rhyodacitic domes and flows, datation of mineralization on adularia sericite	Ag–Bi–Pb–Cu–W–Au		Post	Petersen et al. (1977)
USA, CO	Creede	26.6	24	2.0	San Juan volcanic field: voluminous ash-flow tuffs between 30 and 26 Ma. Cluster of ash-flow calderas with associated mineralization	Pb–Ag–Zn–Au	26–24	Syn-Post	Bethke and Lipman (1987); Lipman (1997)
	Lake City	22.5	15 × 10	> 1.0?	Nested within the Uncompahgre caldera (28 Ma) Resurgent doming. Quartz-latite flow dome 18.5 Ma: emplacement of rhyolitic intrusions	Pb–Ag–Au	27.5–18.5	Pre–Syn-Post	Slack (1980);
USA, NM	Bursum/Mogollon	29–28	40 × 30	1.0	Rhyolitic flows while subsidence continues 26–23 Ma: fracture rhyolitic volcanism, resurgent uplift (1000 m), and bimodal volcanism.	Pb–Zn–Ag	17–18	Post	Ratté et al. (1984)
USA, NM	Valles/Cochiti	1.1	22 × 20		13 0.1 Ma: Jemez volcanic field; several calderas since 1.75–Ma; then resurgence, small volumes of rhyolitic domes and flows, from 1.0 to 0.1–Ma	Au–Ag–Mo	6; 0.6	Pre and Post	Goff and Gardner (1994)
USA, UT	Mount Belknap	19	17 × 13		Marysvale volcanic field; 21–Ma: domes and flows (east); 20–Ma: eruptions migrated southwest;	U–Mo	13–10	Post	Cunningham and Steven (1979)

Table 1 (*continued*)

Country/state	Caldera/deposit	Age of caldera (Ma)	Diameter (km)	d[a] (km)	Chronology of magmatic events	Mineralization	Ages (Ma) of mineralization	Pre/Syn or post- caldera mineralization	Ref.
High sulfidation epithermal ore deposits									
CHILE	El Indio	13.7	8 × 3.5	0.7–2.5	13.7–Ma: andesitic unit surrounding EI Indio 13.4–8.6 Ma: altered ignimbrites and tuffs which host the mineralization	Au–Cu–Ag–As	13.4–8.6	Post	Jannas et al. (1990)
RUSSIA, (Kamchatka)	Uzon	Upper Pleist.	10 × 7	> 1.0?	Series of explosive eruptions: ignimbrites then caldera collapse; 12 ka: dacite extrusion. Contrasting magmatism from Pleist. to Holoc.	As–Sb–Hg–(Au–Ag)	Still active	Still active	Karpov and Naboko (1990)
SPAIN	Rodalquilar and Lomilla	11.1	8 × 5	1.0	15–7 Ma: Capo de Gata volcanic field	Pb–Zn–Au–Ag	11.3–9.5	Pre–Post	Arribas et al. (1995a); Rytuba et al. (1990)
		11.0–10.0	2 × 1	0.1	11.2 Ma: Precaldera dacite domes, then eruption of the Cinto ash-flow Tuffs; resurgence. Eruption of Lazaras ash-flow Tuffs and collapse of the embedded Lomilla caldera				
USA, CO	Summitville	29.5	12 × 8	> 0.5?	San Juan volcanic field; caldera filled with ash-flow tuffs (30–28 Ma) then with andesite (26.6 Ma) Important post-caldera activity (between 29 and 20 Ma): porphyritic rhyodacitic and rhyolitic lavas; granitic stocks; porphyry intrusion at depth	Au–Ag–Cu	22.4	Post	Gray and Coolbaugh (1994)
Porphyry-type ore deposits									
RUSSIA, (Caucasus Mountains)	Chegem-Eldjurta	2.8	15 × 11	> 2.0?	Caldera filled with rhyolitic to dacitic welded tuff; intrusion of a granodiorite porphyry. The exposed Eldjurta granite and Chegem caldera could belong to the same batholith at depth.	W–Mo	4.3 and after	Pre–Post (?)	Lipman et al. (1993); Gazis et al. (1995)
USA, AZ	Silver Bell	73–69	> 8		Postcollapse andesitic flows; late ring-fault; intrusions host the mineralization	Cu		Syn-Post (?)	Lipman (1984); Lipman and Sawyer (1985)
USA, NM	Questa	26–18	> 15		Continuous magmatism? cluster of small magma chambers; slow cooling; underplating?	Mo		Post	Lipman (1984); Lipman (1992)

[a] Thickness of deposits; some information on the pre/syn/post caldera mineralization ages are deduced from field observations.

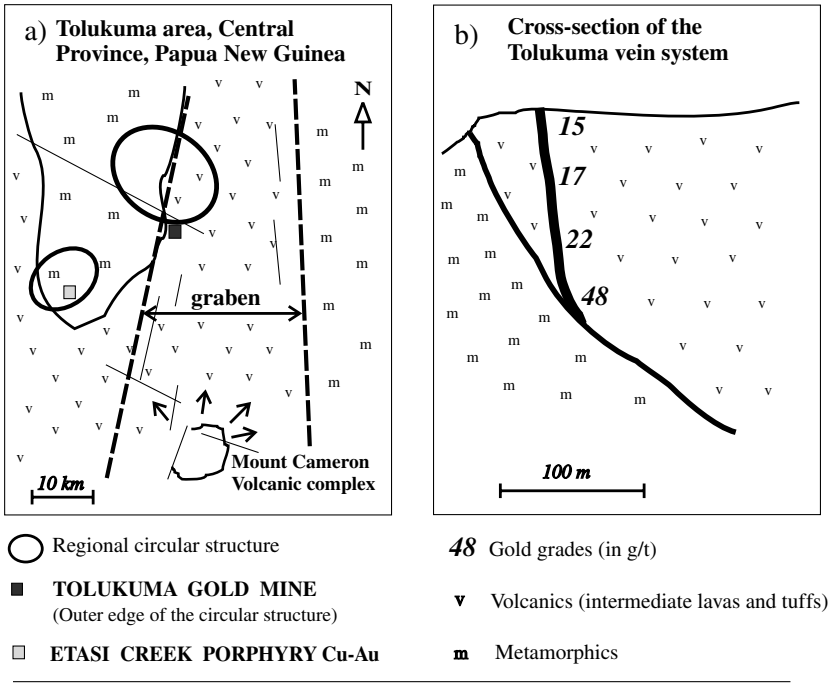

Fig. 1. Simplified sketch of the Tolukuma gold deposit, Papua New Guinea, after Semple et al. (1998). (a) Regional setting, showing the graben and two circular structures. The epithermal gold deposit is located at the outer edge of one circular structure. Note the presence of a porphyry-type deposit within the other, about 20 km away. (b) Cross-section of a mineralized vein, with gold grades increasing with depth. Note the "Y-shape" of this fault system.

consideration. The roles of magma chamber aspect ratios and regional stress regimes have also been investigated.

3.1. Mechanical model and numerical procedure

In our previous study (Burov and Guillou-Frottier, 1999), hereafter noted "BG", we developed an analytical and numerical thermo-mechanical model of caldera formation, based on brittle–elasto-ductile rheology, that accounts for contrasting thermal conductivities of caldera-related rocks. During our experiments, the magma chamber aspect ratios (width to thickness) were varied from 1 to 15, which enabled us to establish critical aspect ratios at which caldera collapse and border faulting may be initiated. It is a fully two-dimensional (no axial symmetry) model that allows for asymmetric behavior. Faults are not a priori defined but are created during computations, thanks to the ability of the adopted numerical algorithm to reproduce brittle localization (see below). Magma is assumed to be evacuated from a shallow silicic magma chamber (2–5 km depth) through a central vent (constant chamber overpressure). The magma is then transformed into low density and low thermal conductivity ignimbrites (ash-flow units) within the forming caldera (Fig. 2). The explosive eruption is not modeled, but accounted for by equivalent material outflow from the chamber to the caldera. This simplification is justified by the fact that we are only interested in the long-term evolution of the system. The calculations provide stress and thermal regimes versus time around the magma chamber and its vicinity, prediction of fault location and geometry, and directions of the potential brittle failure zones around the magma reservoir. Details concerning the numerical procedure (PARAVOZ code (Poliakov et al., 1993) derived from a FLAC®

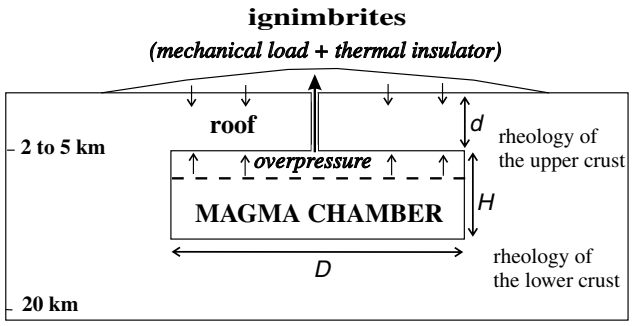

Fig. 2. Sketch of the thermo-mechanical model (described in Burov and Guillou-Frottier, 1999) showing initial and boundary conditions. Dynamic equations of motion and heat equations are simultaneously solved for the whole domain (see Appendix B). Solutions are given in terms of stress distribution (second invariant of the shear stress), fault localization (accumulated plastic strain), directions of potential brittle failure, and temperature field.

algorithm (Cundall, 1989), boundary and initial conditions, and numerical model set-up can be found in the BG paper. The basic hypotheses are described in Appendix A.

We consider two different scenarios. (1) Caldera collapse assuming an existing magma chamber with a pre-defined rectangular chamber geometry. For most experiments, we assumed a steady-state geotherm and no heat transport during the collapse stage, although some were carried out in the fully coupled thermo-mechanical mode. (2) A fully coupled thermo-mechanical model taking into account the final stages of chamber emplacement within the upper crust, surface uplift and subsequent subsidence, although no magma eruption was imposed. In this second scenario, we implicitly assume a light, i.e. gravitationally unstable, magmatic body which settles at shallow levels. Magma ascent continues until either (a) gravitational equilibrium with the surroundings is reached, (b) the magma chamber is faced with a strong rheological barrier, or (c) the thermal energy stored in the body is capable of maintaining the magma and its direct vicinity hot and sufficiently weak (or any combination of the three). Although other ascent mechanisms could have been considered, this one was selected because it allows us to investigate the effects of the final stage of magma chamber emplacement. Results from this second scenario are described in Section 4. Some of the results obtained from simple analytical analyses and from a series of numerical experiments, explained in the BG paper, are presented below.

3.2. Location and geometry of caldera-related faults

The cumulative thickness of intracaldera units commonly exceeds 1 km (see Table 1). For large and shallow silicic magma chambers, such normal loads on the magma chamber roof trigger faulting of the cover above the edges of the reservoir. In our model, “large and shallow” means magma chambers located a few kilometres below the surface, typically 2–5 km, and a reservoir diameter of about 10–15 km. Because in ash-flow calderas, the depth of silicic magma chambers does not vary as much as their diameters, we used a fixed depth of 2.5 km for all the experiments.

The assumed geometry and the rheological and lithological properties are summarized in Fig. 2. A two-layer structure was assumed for the crust. The material leaving the magma chamber through the central vent creates a positive load on the caldera roof and acts as a thermal insulator when deposited. In the experiments with a rectangular magma chamber, we used an overpressured (10 MPa) reservoir with a varying caldera aspect ratio (diameter/depth to magma chamber roof, D/d). As shown in the BG paper, initialization of border faults is essentially controlled by the value of D/d, with $D/d > 5$ being sufficient for the formation of symmetrical border faults.

Figs. 3 and 4 summarize the results of the first set of experiments assuming a steady-state geotherm and a rectangular magma chamber. During the uplift stage (Fig. 3), overpressure in the magma chamber results in

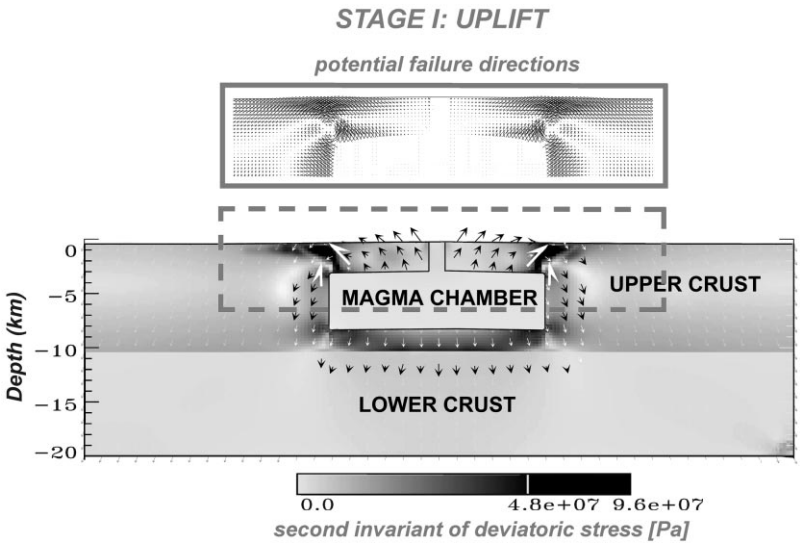

Fig. 3. Bottom: Caldera uplift stage resulting in failure of the magma chamber roof and formation of border faults. Due to the elongated shape of the magma chamber, stresses are concentrated at the sides and primary inclined faults are created. Arrows correspond to velocity vectors. Top: Zones of potential failure predict the distribution of micro fractures. The potential fracture density is most marked at the outer edge of the subvertical fault, as well as near the rounded edges of the magma chamber.

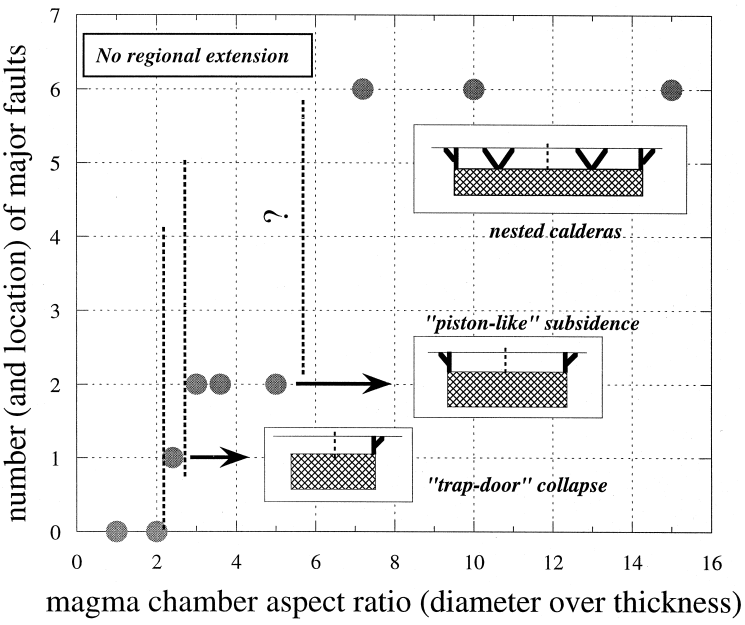

Fig. 4. Summary of the results obtained from the numerical simulations when no regional extension is applied. The number and location of the major faults are recorded as a function of the magma chamber aspect ratio *D/H* (diameter over thickness). In these calculations, the magma chamber roof is at a depth of 2.5 km below the surface.

flexural uplift of the caldera roof causing bending stress to be concentrated along the vertical sides of the roof. This results in strain localization, brittle failure and border faulting (Burov and Guillou-Frottier, 1999). Two groups of faults are predicted by the model: inclined primary and subvertical secondary faults (top of Fig. 3). Inclined border faults are initiated during the flexural stage, whereas subvertical faults are formed when the magma is extruded onto the roof surface, causing overloading and subsidence. Pressure gradients are also enhanced during subsidence, which favors fluid pumping through fractured and faulted zones (see Section 4).

The results of these experiments (Fig. 4) demonstrate that the number and location of faults clearly depend on the magma chamber aspect ratio. It is shown that for a magma chamber aspect ratio *D/H* (diameter over thickness, where $H = 2d$ in our model) lower than 2.4, no border faults appear because the external load is easily balanced by the strength of the underlying crust. Thanks to the numerical algorithm adopted, without a prescribed geometry, we were able to reproduce asymmetrical faulting behavior (aspect ratio equal to 2.4). When a larger magma chamber aspect ratio was considered, internal embedded faults are created (see Fig. 4 for *D/H* greater than 7). It is thus shown that magma chamber geometry controls the mechanism of collapse. For example, the so-called "trap-door" and "piston-like" collapse mechanisms (e.g. Lipman, 1997) have been successfully simulated with realistic hypotheses for crustal rheology and physical rock properties. Moreover, the presence of internal embedded faults above certain large magma chambers suggests that our scenario is also a plausible mechanism for the genesis of "nested calderas" (Burov and Guillou-Frottier, 1999).

It is noteworthy that secondary inclined faults are commonly initiated at the outer caldera edges, even in the case of the one single-side faulted cover (when $D/H = 2.4$). Such structures (subvertical and adjacent inclined faults) are commonly observed in the field (Buchanan, 1981). Hereafter, these structures will be called "Y-shaped" faults. Subvertical faults on both sides of the system are associated with a subsequent "plate-like" subsidence, whereas the related inclined faults could account for scarp retreat events. However, in some cases, we observe a single inclined fault on one side of the caldera and a "Y-shaped" fault on the other (Fig. 5). The "Y-shaped" border fault geometries are also deduced from field and drilling data of mineralized veins in low-sulfidation epithermal ore deposits (Fig. 1b).

In a series of other calculations, regional extension was applied to the model, which had a significant effect on stress distribution. Assuming a constant regional extension of 10 mm/yr, we observe that caldera border faults are not fully developed because deeper and more numerous faults, centered over the magma chamber roof, are more easily triggered. Fig. 6 shows these two cases, with and without regional extension, for identical magma chamber geometries and other conditions. With time, the number of fractures around the central cluster increases, and the fractured zones propagate towards the edges of the reservoir. Consequently, regional extension within caldera settings tends to favor conditions for deep-seated and intrusion-centered ore deposits.

3.3. Heat refraction around faults

Ash-flow calderas represent specific geological systems such as sedimentary basins, where thermally insulating rocks are embedded in thermally conductive fractured rocks (thermal conductivities k_i and k_f, respectively). Ash-flow units are known to have a low conductivity (Sorey et al., 1991; Clauser and Huenges, 1995; Corrado et al., 1998), whereas fractured rocks, generally enriched with quartz, are undoubtedly more conductive than their host rocks (conductivity k_h). It follows that lateral contrasts in thermal conductivities occur within ash-flow calderas (i.e. in dimensionless values, $k_i < k_h = 1 < k_f$). As analytical modeling of steady-state heat refraction around the caldera border faults is described in the BG paper, we develop below a more complete analysis of heat refraction around conductive faults, whether caldera-related or not, in order to concentrate on the specific heat refraction effects within ash-flow caldera settings (Fig. 7). The first case (a) considers a conductive fault embedded in "normal" host rocks; the second case (b) considers a fault separating two semi-infinite media, insulating on the left (thermal conductivity $k_l < 1$), and "normal" conductivity on the right (thermal conductivity $k_r = 1$); the third case (c) corresponds to the caldera case, where the

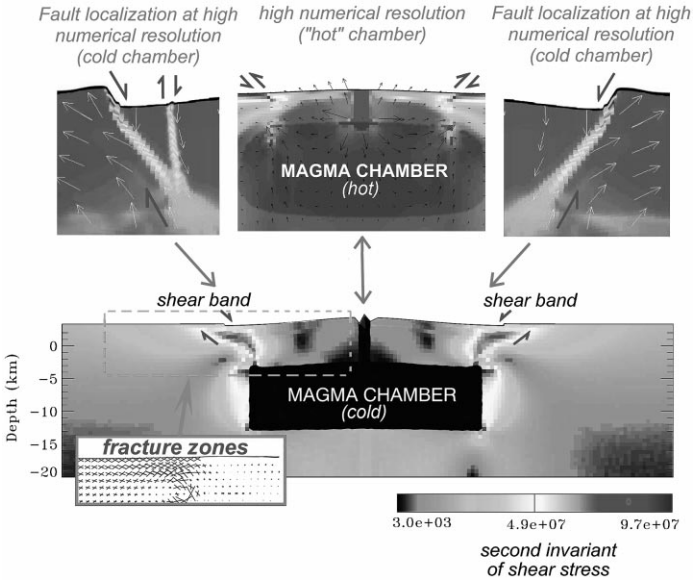

Fig. 5. Snapshot of caldera formation during a thermo-mechanical experiment with high resolution (top). Central top figure shows the case of a fully coupled experiment, where hot magma interacts with its surroundings (see Burov and Guillou-Frottier, 1999 for details). The asymmetrical behavior is evidenced by the "Y-shaped" fault on the left, whereas a single inclined fault is obtained on the right. This type of border faulting process can lead to the so-called "trap-door collapse" mechanisms.

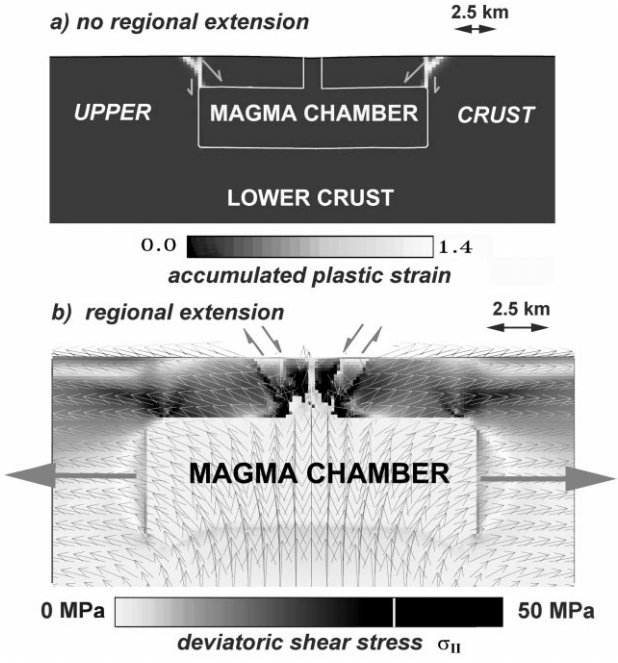

Fig. 6. Fault localization for a given magma chamber aspect ratio of 2.5, without (top) and with (bottom) regional extension. Border faults are well defined in the top figure (showing accumulated plastic strain, i.e. fault localization), whereas they almost disappear in the presence of a regional extension (bottom figure, showing second invariant of shear stress).

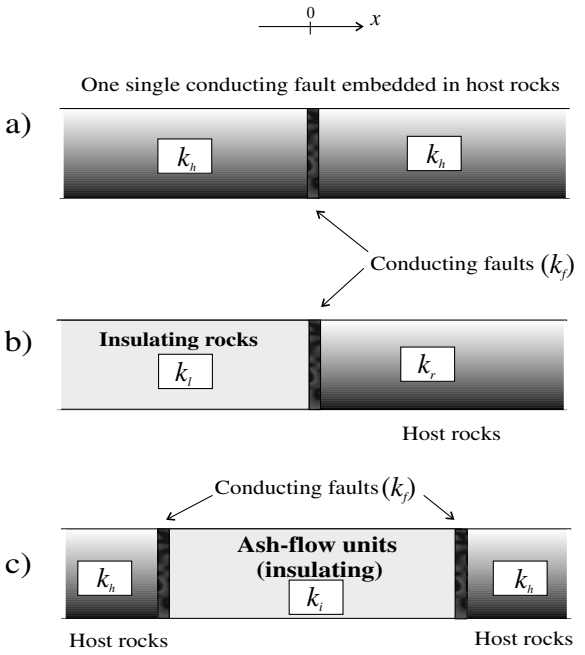

Fig. 7. Sketch of the three models used for studying heat refraction effects around faults: (a) a single fault embedded in an infinite plate of "normal" conductivity; (b) same as the previous case but the medium on the left is insulating; (c) the insulating medium is of finite size (caldera case) and the embedding medium (plate) is infinite.

insulating medium is of finite size. Boundary conditions and analytical solutions of the steady-state heat equation are described in Appendix A. Briefly, the results simply show that the different configurations led to different heat transfer mechanisms, the most important effect for this study being due to the finite size of the caldera.

Fig. 8 shows that lateral heat transfer is induced by the presence of a conductive fault, although a negative heat flow anomaly is observed at the outer edges of the faults in case (a). The highly conductive fault distorts the isotherms with depth, with a consequent decrease in temperature gradients inside and outside the fault. In case (b), the fault is again adjacent to lower conductivity rocks, but the insulating medium on the left side raises the isotherms, allowing for the heat excess to be transmitted laterally across the fault. The medium on the right shows a positive anomaly (temperature gradients and heat fluxes greater than 1), which decreases regularly with depth. In case (c), the accumulated heat within the insulating medium of finite size (intracaldera units) causes, at depth, a lateral heat transfer from the centre of the caldera outwards. A positive and deep-seated heat flow anomaly is thus observed near the outer edge of the caldera-related fault, contrary to the two previous cases. Note that the fault width in Fig. 8 is exaggerated to emphasize the differences between these heat transfer mechanisms. Fig. 9 shows vertical profiles of heat flow variation with depth along the outer right side of the fault. Note the positive and localized anomaly of the third case ("+" in Fig. 9).

The results show that in the caldera case (c), a thermal anomaly (vertical heat flow excess) develops at depth along the outer sides of the conducting fault (Fig. 8c). Since a fixed temperature condition is present at the surface, the heat that accumulated within the poorly conductive intracaldera rocks of finite size cannot distort the isotherm much. Rather, the excess heat is easily transferred laterally at depth, and for relatively large fault widths, i.e. efficient heat conductors (Burov and Guillou-Frottier, 1999). However, it is shown in the BG paper that this anomaly is primarily controlled by the conductivity of the intracaldera units, k_i, which can be ten times lower than that of the faulted rocks. In the first two cases, the infinite media surrounding the fault have a diminishing effect on any strong heat refraction, allowing the fault to "pump" any excess heat.

3.4. Thermo-mechanical coupling and favored areas

In the previous numerical modeling (Figs. 3–6), thermal effects were not taken into consideration, such as heat diffusion from the magma reservoir or heat refraction due to the presence of both insulating ignimbrites and conductive fractured rocks. Some interesting new features appeared when these processes were added to the numerical code. Although the location of the border faults was not significantly changed, their geometry was affected by temperature-dependent rheology. The insulating cover tends to heat the underlying system and thus raise the isotherms. It follows that the brittle–ductile transition (BDT) zone, which is commonly assumed to represent the 300–400°C temperature range, is also uplifted and exhibits a sigmoid shape in the vicinity of the magma reservoir, as suggested by Hill et al. (1998) for the

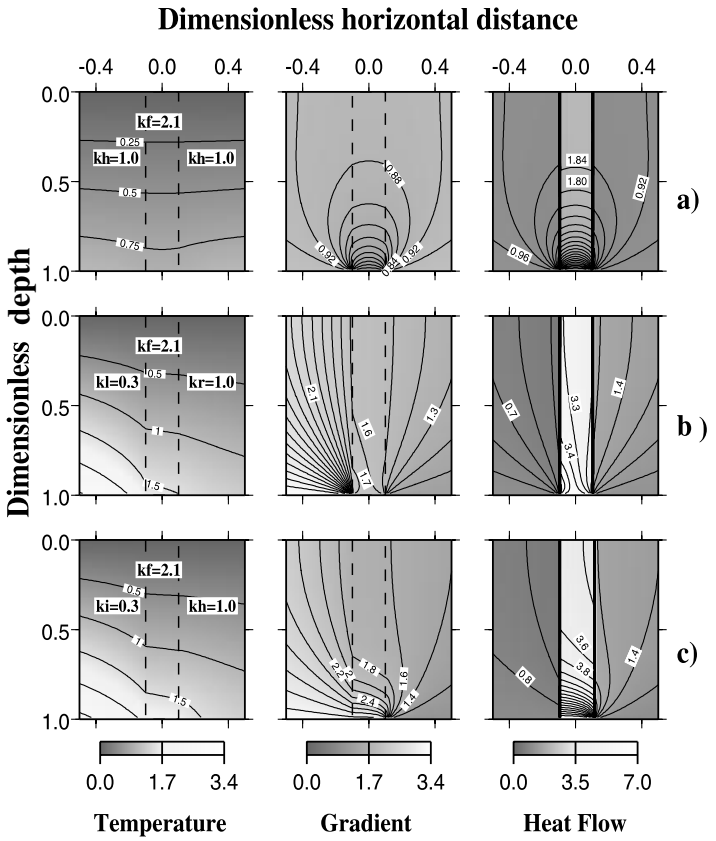

Fig. 8. Results from analytical solutions developed in Appendix A for the three cases of Fig. 7. Top, middle and bottom rows correspond to cases (a), (b), and (c), respectively. Note the positive anomaly at depth for the caldera-related fault (case c).

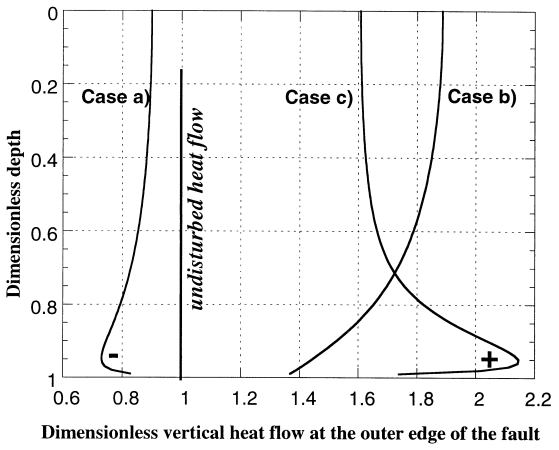

Fig. 9. Details of the vertical heat flow profiles at the outer edge of the conducting fault for the three cases of Fig. 7. Note the anomalous positive heat anomaly at depth, for case (c).

Long Valley Caldera in California. Our model shows, however, two additional features: (1) the BDT is marked by a subhorizontal fracture zone in the middle of the cover, thus delineating a "mechanical magma chamber"; (2) lateral border faults are inward-dipping at the surface but outward-dipping at depth. As emphasized in the BG paper, the location and geometry of these faults (inclined border faults and subhorizontal faults) is almost identical to the earthquake distribution recorded by Jones and Stewart (1997) at the Rabaul caldera, Papua New Guinea. In addition, the density of second-order cracks appears to be highest at the outer sides of the subvertical border faults, thus enhancing their structural "trapping" capabilities (see also the constant temperature case in Fig. 3, where potential brittle failure zones are concentrated at the caldera borders).

3.5. Variations in lithostatic pressure and fluid circulation during the syn- and post-collapse stages

Without regional extension. As can be seen in Fig. 10, non-lithostatic pressure variations on the magma chamber roof and in the vicinity of the border faults can reach 10–20 MPa, with deep overpressured zones close to the inner edge of the chamber corner and shallow underpressured zones in the vicinity of the inner sides of the faults. Consequently, the fluid is likely to be pumped from the upper outer zones of the faults (A′) to the upper inner zones (C and A), as well as from the roof/chamber interface zone (B) towards the deep outer zone (B′). Without considering the potential fracture density, one could also propose a fluid flow from the deep inner zone (B) towards the upper inner zone (A), as well as from (A′) to (B′). However, fluid flow paths and intensity are conditioned by fracture density, which is likely to be highest in the upper parts of the outer zone A′, in between the inclined and vertical fault (C), and in the lower inner part (B) of the fault (Figs. 3 and 5). Thus, zones A′, C and B should be most favorable for intensive flow and heat exchanges and, consequently, for mineralization.

With regional extension. In the presence of far-field extension (Fig. 6), the border faulting associated with flexure of the chamber roof is attenuated by the stress. This leads to concentrated faulting and pressure variations in the central areas. In this case, the most intensive fracturing and fluid circulation will be concentrated in the central vent zone, thus favoring porphyry-type mineralization.

4. Formation of pre-collapse mineralization traps

A number of ore deposits hosted in ash-flow calderas predate the caldera collapse, as shown in Table 1. As stated above, we believe that mineralization depends firstly on the presence of thermal and structural traps. Fluid–rock interactions cannot lead to mineral deposition outside particular zones where heat and mass exchanges can occur.

It has been shown that the insulating intracaldera units tend to increase lateral heat transfer towards the border faults. Along the outer sides of the border faults, a combination of thermally anomalous areas and a high fracture density improves the “trapping” capabilities of these zones. However, before explosive eruption and caldera collapse, and thus pre-deposition of a thick insulating cover, no blanketing effect exists, and there is no reason a priori for preferential mineralization in the vicinity of the rounded edges of the magma chamber. Nevertheless, field data and geochronological data seem to indicate that pre-collapse mineralization stages do

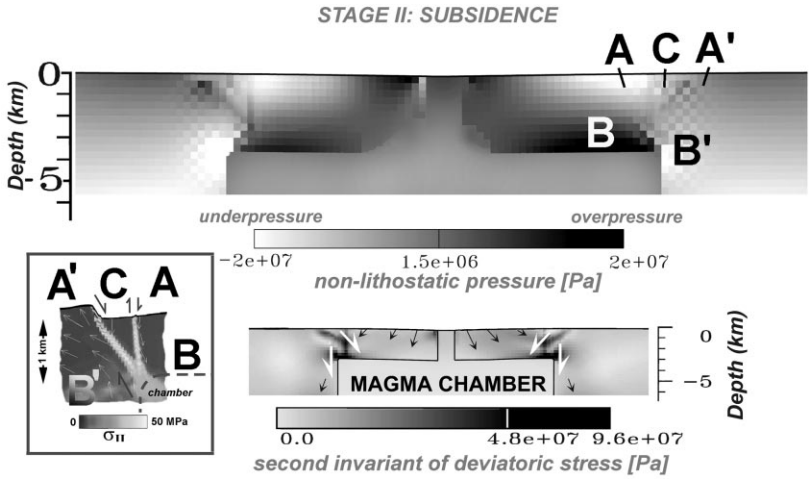

Fig. 10. Caldera collapse stage (bottom) and associated non-lithostatic pressure distribution (top). Black and white areas correspond, respectively, to overpressured and underpressured zones, meaning that fluid tends to flow from black to white areas. Fives zones are delineated (A, A′, B, B′, C) depending on their positions with respect to faulted zones (see inset) and depth. Fluid trapping capabilities are explained in the text.

occur in some large ash-flow calderas. Fig. 11 shows a series of geochronological data taken from the literature concerning mineralized ash-flow calderas, plotted against the caldera area. Both porphyry-type and epithermal deposits have been included in this plot in order to emphasize the existence of pre-collapse mineralization within ash-flow caldera settings, whatever the type of deposit. According to Fig. 11, it seems that small calderas do not contain pre-collapse mineralization. One could argue that pre-collapse mineralization needs the presence of faults during an early stage of magmatic evolution, before the caldera formed. In this case, the heat source would be the magma itself, but some explanation is required for pre-collapse faulting of the overlying crust. This plot suggests that pre-collapse faulting of the crust would only occur for large magmatic bodies, thus creating sufficiently high stresses in the upper brittle crust, whereas small magma chambers would cool before the reservoir settled within the upper crust.

A new mechanism acting prior to the eruption

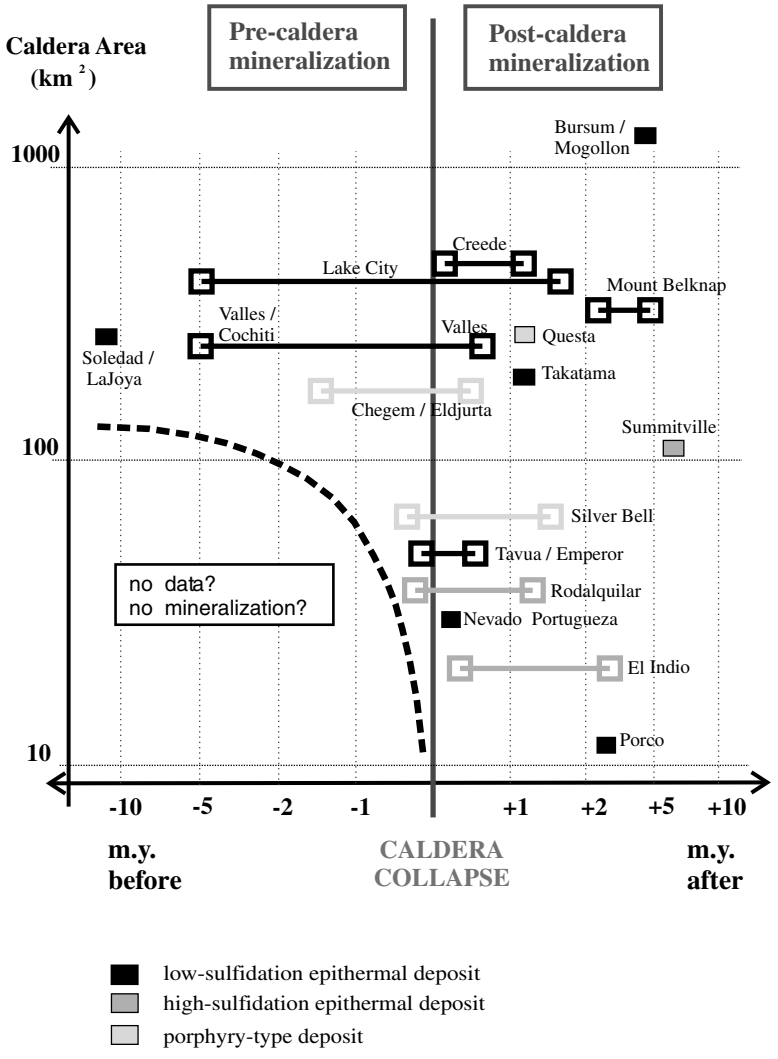

Fig. 11. Geochronological data taken from 16 mineralized ash-flow calderas. No pre-collapse mineralization is documented for small calderas, whereas several large ash-flow calderas show pre-collapse mineralization. According to this plot, the content of which is not exhaustive, caldera size may play a role in pre-collapse mineralization processes.

phase could explain pre-caldera mineralization. When large and hot silicic magma chambers settle at shallow crustal levels, the hot magma significantly disturbs the thermal regime of the crust, and thus its stable stratified rheology. The magma chamber roof is deformed and the BDT zone is raised around the reservoir, delineating the "thermo-mechanical geometry" of the magma chamber. It follows that the upper crust forms a thinned brittle layer above the reservoir, which becomes more and more elongated. Fractures and cracks are thus more easily initiated within this layer.

The second set of experiments was intended to investigate a number of phenomena that can precede magma chamber emplacement and caldera collapse. The detailed investigation of possible emplacement mechanisms is largely beyond the scope of this study and would require in itself an individual study. For this reason, we decided to focus our analysis to the thermo-mechanical consequences of emplacement and thus only consider a simplified hypothetical situation, in which an initial spherical magma chamber, deeper than its final emplacement depth, ascends under positive buoyancy forces (e.g. Chandrasekhar, 1981). In reality, the chamber may be emplaced in a different way, but it is clear that any density changes in the already formed magma body will result in stress exertion on the surrounding rock. Depending on the density contrast and the mechanical resistance of this rock, the chamber should deform or move up and down to minimize the stress difference. With time, heat diffusion from the reservoir to the surrounding crust has two major consequences. The first is weakening of the magma chamber envelope, facilitating vertical movement of the magma body and the second is cooling of the reservoir leading to a higher magma viscosity at the boundaries and thus greater resistance to vertical displacement. We performed several series of calculations with large reservoirs, which show that the minimal emplacement depth of sufficiently hot magmas (around 800°C) is limited to 2–5 km by the near-surface thermo-mechanical barrier at BDT, whatever the positive density contrast is. It is noteworthy that most silicic magma chambers below ash-flow calderas seem to have settled within this depth range. This result suggests that silicic magma chambers may have a positive density contrast with the host rock. Consequently, this result has very important implications for magma chamber settlement for it shows that the gravity is not the only controlling force for locking magma chambers within the upper crust (Ryan, 1987). It supports recent ideas concerning the active role of tectonic regimes in the emplacement depths of magmas (Watanabe et al., 1999).

Fig. 12 shows that the viscous stress created by a buoyant magma chamber can result in brittle failure in the upper crust associated with extension and upward bending resulting from stress-induced flow (Fig. 12, bottom). The brittle strength of the rocks is low during extension, meaning that the crust may be easily broken, and that surface normal faults can appear well before the final emplacement of the chamber near the surface. It is possible that these faults may serve as hydrothermal fluid channels, thus explaining appearance of pre-caldera mineralization, as it might be the case for the Martha Hill gold-silver deposit, Waihi, New Zealand (B. Brathwaite, personal communication; Brathwaite and McKay, 1989). The distance between the primary normal faults is largely controlled by the effective thickness of the brittle layer and to a lesser degree by the size of the magma chambers itself. However, during the later stages when the upper crustal layer and magma chamber cool down and subside, a second group of faults (Fig. 12, top) may appear, this time corresponding to the chamber borders.

In all cases, we observe strong pressure gradients from the center of the chamber roof towards the borders, as well as fault-induced pressure gradients. Active faults may be associated with high local pressure due to shearing on fault surfaces. The internal fault geometry defines the direction of pressure gradients associated with the fault (see the "valve effect" described by Sibson, 1987). The pressure is higher along the narrow parts of the fault and lower along its wider parts; lithostatic pressure increases with depth and thus should be added to or subtracted from the valve effect. Nevertheless, the inclined downward-widening faults, as shown in Fig. 12, may pump fluids downwards and outwards, whereas the vertical faults may pump them upwards, thus forming a kind of a circulation loop through the "Y-shaped" double fault system. As mentioned earlier, fluid paths cannot be realistically predicted without coupling the mechanical solution with

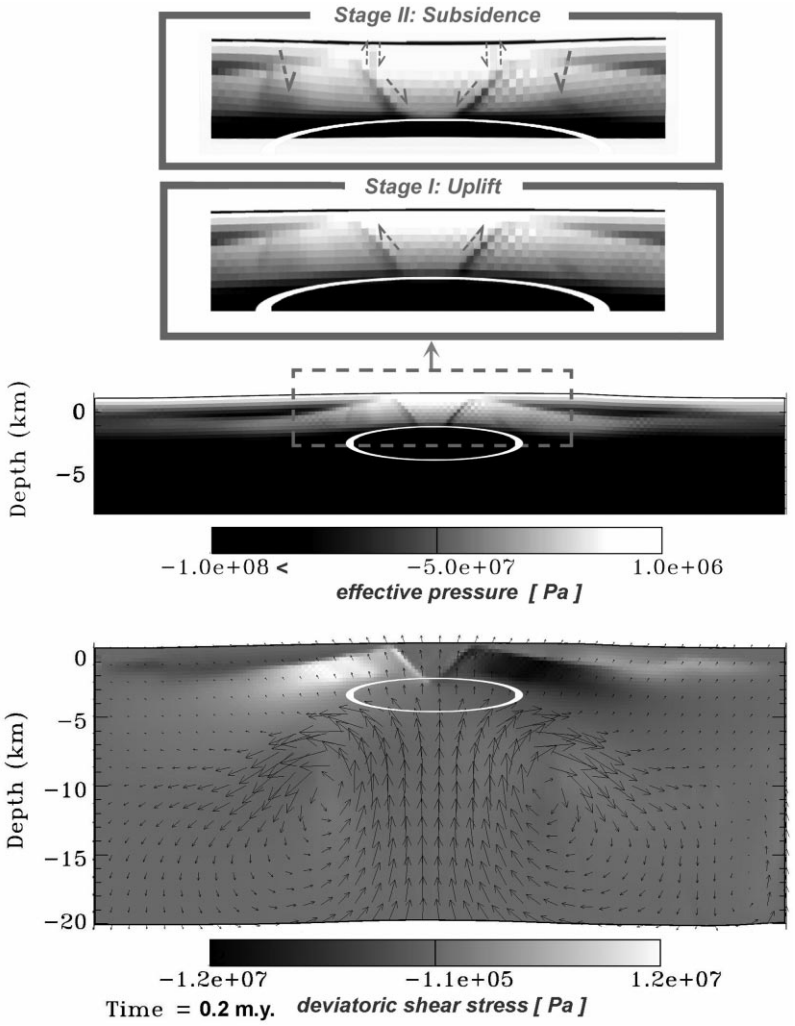

Fig. 12. Emplacement of a magma chamber resulting in surface bulging and pre-volcanic faulting followed by subsidence.

fluid-flow solution through a permeable matrix. However, the highly variable parameters of such a matrix would be difficult to define, and some authors have shown that fault-induced pressure gradients may dominate over other mechanisms (Y. Podladchikov, personal communication). Our approach, based on the calculation of pressure gradients and the prediction of crack concentration zones, may provide a reasonable first approximation.

Despite the absence of surface loads (no eruption in these simulations), the magmatic overpressure tends to focus the shear stress and the major deformation structures in the vicinity of the rounded edges of the reservoir, thus creating “pre-eruptive” border faults within the brittle part of the upper crust. In addition to these “pre-eruptive” border faults, we observe the formation of a subhorizontal fault, corresponding to the horizontal portion of the BDT zone (above the magma chamber roof), and thus representing another possible fluid pathway. This “pre-cutting” of the upper crust may favor a particular style of collapse once explosive eruption occurs. It may also promote preferential pathways subsequently followed by hydrothermal fluids.

The major result here is related to the pre-existence

of structural traps before eruption and thus before caldera formation. At that time, the heat source is clearly present because the magma has not cooled sufficiently to be frozen by the surroundings. It follows from these experiments that thermal and structural traps can be formed long before caldera collapse. Numerous field examples show that eruptions of several rhyodacite domes along border faults predate caldera collapse (see Table 1). These pre-caldera eruptions could indeed be facilitated by pre-collapse faults, allowing highly silicic and viscous magma to escape easily to the surface.

5. Discussion and conclusion

Several authors have investigated the mineral potential of ash-flow calderas, but the genetic link between the ore deposits and caldera formation remains controversial. Field observations over several decades have shown that ash-flow caldera features (e.g. the presence of ignimbrites and ring faults) represent a kind of exploration guide for mining geologists. However, it is often difficult to recognize ash-flow caldera signatures in the field because of intensive erosion probably related to the proximity of subduction zones. Our results have shown that the location and distribution of traps for ore deposits strongly depend on large-scale factors, such as magma chamber geometry and regional tectonics. Therefore, it seems useful to incorporate these large-scale factors and the long-term evolution of calderas into mineral exploration strategies.

Favorable areas, i.e. the outer sides of the border faults, have been described in terms of steady-state heat refraction effects, density of potential brittle failure, and thus potential hydrothermal fluid pathways. Our study evidently lacks fluid dynamics within such systems, and fluid geochemistry in the presence of an anomalous thermal field. As such an approach would need to take into account so many other parameters (fluid properties and compositions, rock porosities and permeabilities, etc.), we decided to first restrict this new thermo-mechanical modeling to a simple and unresolved problem. Despite the absence of fluids, "Y-shaped" border faults of ash-flow calderas have been obtained and because these geometries are common in mining districts, our modeling approach seems to successfully reproduce the basic principles of the thermo-mechanical processes associated with caldera settings.

According to our results, the conditions for epithermal gold mineralization (high and low sulfidation) can switch to those for porphyry mineralization under the influence of regional extension. In subduction-related volcanic settings, this regional change is very likely to occur because the amount of retrograde motion of subduction zones as well as the dip angle of subducted slabs can undergo marked changes over a few million years (Garfunkel et al., 1986; Sillitoe, 1989; Guillou-Frottier et al., 1995).

The most intriguing result of our modeling remains the "pre-cutting" of the upper crust when silicic magma chambers settle at shallow depths. It seems that faulting conditions for caldera collapse might be conditioned by the pre-eruptive history of the magmatic system. The amount of overpressure needed to lead to the development of pre-eruptive faults should be easily reached with large and voluminous magma reservoirs. In consequence, pre-collapse mineralization would only occur for large caldera areas, as suggested in Fig. 11.

Another surprising phenomenon is a juxtaposition of some low/high sulfidation ore deposits with porphyry-type ore deposits (e.g. Sillitoe, 1994; Arribas et al., 1995b). Erosion would be the driving mechanism, enabling deep mineralization to "telescope" ore deposits forming at the surface. Implicitly, the deep mineralization brought to the surface is either pre or syn with respect to the shallower ore deposits. Erosion has been demonstrated to act as a major process affecting — in a subtle way — both the thermal and the mechanical regimes of the crust (e.g. England and Richardson, 1980; Avouac and Burov, 1996), although it is not clear whether erosion would tend to favor or inhibit mineralization potential. Our results on potential fracture distribution and subsequent potential fluid pathways (Section 3.5 and Fig. 10) suggest that shallow and deep mineralization located above magma chamber corners could telescope if the potential failure zones above the magma chamber borders were not eroded. Such complex interactions between caldera evolution over a few m.y. combined with a high erosion rate must be investigated in the future.

Acknowledgements

This paper has greatly benefited from the ideas of and discussions with Bob Brathwaite, Eric Marcoux, Alexis Poliakov and Yuri Podladchikov. We thank P. Browne and G. Bergantz for their constructive reviews. We would like to thank Rowena Stead for proofreading the final text and English editing. This is BRGM publication 45.

Appendix A. Heat refraction around conductive faults

To compute the thermal field in the three cases of Fig. 5, we have solved the heat diffusion equation in steady-state using a Cartesian geometry. In the three cases, the following dimensionless boundary conditions apply: (1) a fixed temperature ($T=0$) is imposed at the surface ($z=0$); (2) a constant heat flow ($=1$) is imposed away from the fault (at $x \rightarrow \pm\infty$); (3) temperature increases with depth. For the third case (caldera-related faults), the same constant heat flow value ($=1$) is assumed to be recovered at the center of the caldera ($x=0$). This condition is equivalent to a "large caldera" hypothesis, meaning that heat refraction effects are restricted to the direct vicinity of the fault. By continuity of temperature and horizontal heat flow through the vertical interfaces (fault sides), an analytical solution is obtained for the thermal field. Various fault widths and conductivity values have been tested (see details for the third case in the BG paper).

The steady-state heat equation in Cartesian geometry writes:

$$\Delta T(x,z) = 0 \tag{A1}$$

where T is the temperature, x the horizontal distance and z the depth. At the surface, temperature equals zero whatever the medium considered:

$$T(x,\ z=0) = 0 \tag{A2}$$

Farther away from the fault, at $x \rightarrow \pm\infty$, temperature must tend to 1 for $z \rightarrow 1$, a consequence of the vanishing heat flow perturbation. This condition can be written:

$$\lim_{x \rightarrow \pm\infty} T(x, z \rightarrow 1) = 1 = k_j \times \frac{\partial T}{\partial z}(x \rightarrow \pm\infty, z=0) \tag{A3}$$

k_j being the thermal conductivity of the medium considered (e.g. $k_h = 1$ in the first case). Finally, in the three cases, temperature must increase with depth:

$$\frac{\partial T}{\partial z}(x,z) > 0 \tag{A4}$$

For the third case, one condition is missing for solving the heat equation: we have imposed a final condition at the surface and at the center of the caldera:

$$\lim_{a \gg 1} k_i \left(\frac{\partial T}{\partial z} \right)(x=0, z=0) = 1 \tag{A5}$$

where a is the inner radius of the caldera (i.e. the horizontal distance from the center of the caldera to the inner side of the border fault). This condition is valid only for large calderas. Isotherms are thus locally disturbed by the fault, but the constant heat flow is recovered at the center of the caldera, as soon as caldera size is sufficient. For a representative conductivity ratio $k_f/k_i = 4$, and for a caldera size equal to 4 ($a=2$), the error is less than 3%.

Solutions for temperature distribution, vertical gradient and vertical heat flow are expressed with Fourier series. In the case where the host rocks surround a single fault (case a), temperature outside the fault can be written as:

$$T(x,z) = \sum_m a_m \exp(-q_m|x|) \sin(q_m z) + \sum_m \alpha_m \sin(q_m z) \tag{A6}$$

where q_m are wave numbers, and where a_m and α_m are the Fourier coefficients to be determined. In the three cases, and within each area of Fig. 5, the wave number q_m is determined with the first boundary condition and condition (A4):

$$q_m = \frac{(2m+1)\pi}{2} \tag{A7}$$

In the following, the Fourier series are written as:

$$T(x,z) = \sum_m \sin(q_m z)(d_m f(x) + \lambda_m) \tag{A8}$$

where d_m and λ_m are the unknown Fourier coefficients. The second terms (with Greek symbols) correspond to constant gradients within the intracaldera units (case c) and at the outer sides of the faults (cases a and b). By definition, the constant heat flow condition (A3), when $x \rightarrow \pm\infty$, is recovered with:

$$f(x) = \exp(-q_m|x|) \qquad \text{and with}$$
$$\lambda_m = \frac{8(-1)^m}{\pi^2(2m+1)^2} \times \frac{1}{k_j} \tag{A9}$$

where k_j corresponds to thermal conductivity of the medium (k_h, or k_r, or k_l). For the intracaldera units (case c), the same heat flow is recovered at the center and at the surface of the caldera with:

$$f(x) = \cosh(q_m x) \qquad \text{and with}$$
$$\lambda_m = \frac{8(-1)^m}{\pi^2(2m+1)^2} \times \frac{k_h}{k_i} \tag{A10}$$

To summarize, when continuity of temperature and horizontal heat flow through the vertical interfaces is applied, all Fourier coefficients can be determined. Analytical solutions for the three cases follow:

Case a: a single fault embedded within "normal" rocks.

fault:

$$T(x,z) = \sum_m \sin(q_m z)(a_m f(x) + \alpha_m), \text{ with}$$
$$f(x) = \cosh(q_m x),$$
$$\alpha_m = \frac{8(-1)^m}{\pi^2(2m+1)^2} \times \frac{k_h}{k_f} \qquad \text{and}$$
$$a_m = \frac{\alpha_m\left(\frac{k_f}{k_h} - 1\right)}{\frac{k_f}{k_h}\sinh\left(q_m\frac{w}{2}\right) + \cosh\left(q_m\frac{w}{2}\right)} \tag{A11}$$

where w is the fault width and for a fault centered at $x = 0$.

host rocks:

$$T(x,z) = \sum_m \sin(q_m z)(b_m f(x) + \beta_m), \text{ with}$$
$$f(x) = \exp(-q_m|x|)$$
$$\beta_m = \frac{8(-1)^m}{\pi^2(2m+1)^2} \qquad \text{and}$$
$$b_m = \frac{-k_f}{k_h}\sinh\left(q_m\frac{w}{2}\right)\exp\left(q_m\frac{w}{2}\right)a_m \tag{A12}$$

Case b: a single fault separating host rocks from a semi-infinite insulating medium.

insulating medium (left side):

$$T(x,z) = \sum_m \sin(q_m z)(a'_m f(x) + \alpha'_m), \text{ with}$$
$$f(x) = \exp(q_m x) \tag{A13}$$

fault (middle medium, centered at $x = 0$):

$$T(x,z) = \sum_m \sin(q_m z)(b'_m f(x) + \beta'_m), \text{ with}$$
$$f(x) = \sinh(q_m x) \tag{A14}$$

host rocks (right side):

$$T(x,z) = \sum_m \sin(q_m z)(c'_m f(x) + \gamma'_m), \text{ with}$$
$$f(x) = \exp(-q_m x) \tag{A15}$$

Some coefficients are easily obtained:

$$\alpha'_m = \frac{8(-1)^m}{\pi^2(2m+1)^2}\frac{1}{k_l}, \qquad \text{and}$$
$$\gamma'_m = \frac{8(-1)^m}{\pi^2(2m+1)^2}\frac{1}{k_r}, \tag{A16}$$

and by continuity, the other coefficients can be

written as:

$$b'_m = \frac{\gamma'_m - \alpha'_m}{\left(\frac{k_f}{k_r} + \frac{k_f}{k_l}\right)\cosh\left(q_m \frac{w}{2}\right) + 2\sinh\left(q_m \frac{w}{2}\right)},$$

$$a'_m = \frac{1}{2}\frac{k_f}{k_l}(\exp(q_m w) + 1)b'_m$$

$$c'_m = -\frac{1}{2}\frac{k_f}{k_r}(\exp(q_m w) + 1)b'_m, \qquad \text{and}$$

$$\beta'_m = \gamma'_m + b'_m\left[-\frac{k_f}{k_r}\cosh\left(q_m \frac{w}{2}\right) - \sinh\left(q_m \frac{w}{2}\right)\right] \tag{A17}$$

Case c: the caldera case, where the insulating medium is of finite size.

The solution is similar to the previous ones, except the imposed symmetry at the center of the caldera yields a $\cosh(q_m x)$ term in the series. The reader should refer to the BG paper for the complete solution.

Appendix B. Numerical model and rheological assumptions

Fig. 2 presents the set-up for the different numerical models, for which we adopted a FLAC®-based (Cundall, 1989) finite-element code called "Paravoz" (Poliakov et al., 1993). Paravoz allows for mixed brittle, elastic, viscous and non-Newtonian temperature, stress and strain rate-dependent power-law rheology and complex geometrical structures. This method belongs to the so-called Fast Lagrangian Analysis of Continua family (FLAC®) (Cundall and Board, 1988; Cundall, 1989) of large strain fully explicit time-marching numerical algorithms based on the Lagrangian "moving grid" method. The latter enables the solution of Newton's equation of motion in large strain mode holding a locally symmetric small strain formulation commonly used in continuum mechanics. The major advantage of the FLAC® method is its ability to reproduce initialization and evolution of non-predefined faults, which is crucial given the aims of the present study. This algorithm and its application to caldera modeling are described in detail in Burov and Guillou-Frottier (1999).

The plasto-elasto-viscous finite element Paravoz code (e.g. Poliakov et al., 1993) solves Newton equations of motion in continuum mechanics formulation using the FLAC® method:

$$\rho\frac{\partial v_i}{\partial t} - \frac{\partial \sigma_{ij}}{\partial x_i} - \rho g_i = 0 \tag{B1}$$

where v is the velocity, g the acceleration due to gravity and ρ the density. The FLAC® method uses small strain equations for large strain problems because the numerical mesh moves with the material, and at each time step the new positions of the mesh grid nodes are calculated from the current velocity field and updated in a large strain mode accounting for stress rotation. Solution for velocities at mesh points is used to calculate element strains ε_{ij}. These strains are employed in the constitutive relations yielding element stresses σ_{ij}

Table 2
Parameters of dislocation creep for lithospheric rocks and minerals (The values correspond to the lower limits of the rock strength (Brace and Kohlstedt, 1980; Carter and Tsenn, 1987; Tsenn and Carter, 1987; Kirby and Kronenberg, 1987). The elastic moduli used for all materials throughout this paper are: E (Young's modulus) = 0.8 GPa and ν (Poisson's ratio) = 0.25. The brittle properties are represented by Mohr-Coulomb plasticity with friction angle 30° and cohesion 20 MPa (Gerbault et al., 1998))

Mineral/rock	A^* (Pa^{-n} s^{-1})	H^* (kJ mol^{-1})	n
Quarzite (dry)	5×10^{-12}	190	3
Diorite (dry)	5.01×10^{-15}	212	2.4
Diabase (dry)	6.31×10^{-20}	276	3.05
Olivine/dunite (dry) Dislocation climb at $\sigma_1 - \sigma_3 < 200$ MPa	7×10^{-14}	520	3
Olivine (Dorn's dislocation glide) at $\sigma_1 - \sigma_3 \geq 200$ MPa	$\dot{\varepsilon} = \dot{\varepsilon}_0\exp[-H^*(1-(\sigma_1-\sigma_3)/\sigma_0)^2/RT]$ where $\dot{\varepsilon}_0 = 5.7\times10^{11}$ s^{-1}, $\sigma_0 = 8.5\times10^3$ MPa; $H^* = 535$ kJ mol^{-1}		

and equivalent force $\rho\partial v_i/\partial t$, which provide input for the next calculation cycle. For elastic and brittle materials the constitutive relations have a linear form:

$$\varepsilon_{ij} = A\sigma_{ij} + A_0 \quad \text{(B2)}$$

with A, A_0 being the constitutive parameter matrixes (Table 2). For a ductile rheology, these relations become:

$$\dot{\varepsilon}_{ij} = A\sigma^{n-1}\sigma_{ij} \quad \text{(B3)}$$

where $\dot{\varepsilon}_{ij}$ is the strain rate, $\sigma = (1/2\sigma_{ij}\sigma_{ij})^{1/2}$ is the effective stress (second invariant of the deviatoric stress, as shown in Figs. 3, 5, 6b, 10, 12). The variables n (the effective stress exponent) and A (constitutive parameter) describe the properties of a specific material (Table 2). For ductile materials, n usually equals 2–4 and A is depth and temperature dependent. For brittle and elastic materials, A is usually only depth dependent. Yet, A, A_0 can be functions of strain or stress for softening or hardening materials. To allow for explicit solution of the governing equations, the FLAC® method employs the dynamic relaxation technique based on the introduction of artificial inertial masses in the dynamic system. The adaptive remeshing technique enables the reproduction of strain localization resulting in the formation of faults. The method does not imply inherent rheology assumptions, in contrast to common finite-element techniques.

For an elastic rheology, we use the following constitutive parameters: E (Young's modulus) = 0.8 GPa and v (Poisson's ratio) = 0.25. Brittle behavior is presented by Mohr–Coulomb plasticity with cohesion softening (friction angle 30°, cohesion decreases from 20 MPa at zero strain to 0 at 1% strain (Gerbault et al., 1998)).

Since ductile rheology is temperature dependent, the mechanical balance equations are coupled with heat transport equations:

$$\mathrm{div}(\mathbf{k}\nabla T) - \rho C_\mathrm{p}\partial T/\partial t + H_\mathrm{r} = \mathbf{v}\nabla T \quad \text{(B4)}$$

where $\mathbf{v}$ is the velocity tensor, C_p the specific heat, $\mathbf{k}$ the thermal conductivity tensor, H_r the radiogenic heat production per unit volume. Here we adopted commonly inferred values (e.g. Burov et al., 1993). Technically, the solution of the right-hand side (advective) is separated from the left-hand side (diffusive) part: the former is calculated automatically when solving the equations of motion, whereas the latter is computed using a separate procedure. The size of the mesh elements was between 50×50 m^2 and 250×250 m^2.

References

Ahmad, M., Walshe, J.L., 1990. Wall-rock alteration at the Emperor gold-silver telluride deposit, Fiji. Aus. J. Earth Sci. 37, 189–199.

Anderson, W.B., Eaton, P.C., 1990. Gold mineralization at the Emperor mine, Vatukoula, Fiji. J. Geochem. Explor. 36, 267–296.

Arribas Jr, A., Cunningham, C.G., Rytuba, J.J., Rye, R.O., Kelly, W.C., Podwysocki, M.H., McKee, E.H., Tosdal, R.M., 1995a. Geology, geochronology, fluid inclusions, and isotope geochemistry of the Rodalquilar gold alunite deposit, Spain. Econ. Geol. 90, 795–822.

Arribas Jr, A., Hedenquist, J.W., Itaya, T., Okada, T., Concepcon, R.A., Garcia Jr, J.S., 1995b. Contemporaneous formation of adjacent porphyry and epithermal Cu–Au deposits over 300 ka in northern Luzon, Philippines. Geology 23, 337–340.

Avouac, J.P., Burov, E.B., 1996. Erosion as a driving mechanism of intracontinental mountain growth. J. Geophys. Res. 101, 17747–17769.

Bethke, P.M., Lipman, P.W., 1987. Deep environment of volcanogenic epithermal mineralization; proposed research drilling at Creede, Colorado. Eos Trans. AGU 68 (13), 187–189.

Brace, P., Kohlstedt, D.L., 1980. Limits on lithospheric stress imposed by laboratory modeling. J. Geophys. Res. 85, 6248–6252.

Brathwaite, R.L., McKay, D.F., 1989. Geology and exploration of the Martha Hill gold–silver deposit, Waihi. In: Kear, D. (Ed.), Mineral Deposits of New Zealand, Monograph 13. Australian Institute of Mining and Metallurgy, Melbourne, pp. 83–88.

Buchanan, L.J., 1981. Relations of tectonics to ore deposits in the Southern Cordillera. Arizona Geol. Soc. Digest 14, 237–262.

Burov, E.B., Guillou-Frottier, L., 1999. Thermo-mechanical behavior of large ash-flow calderas. J. Geophys. Res. 104, 23081–23109.

Burov, E.B., Lobkovsky, L.I., Cloetingh, S., Nikishin, A.M., 1993. Continental lithosphere folding in Central Asia (part 2), constraints from gravity and topography. Tectonophysics 226, 73–87.

Carter, N.L., Tsenn, M.C., 1987. Flow properties of continental lithosphere. Tectonophysics 136, 27–63.

Chandrasekhar, S., 1981. Hydrodynamic and Hydromagnetic Stability, 3rd ed. Dover Publications, New York.

Chéry, J., Bonneville, A., Vilotte, J.P., Yuen, D., 1991. Numerical modeling of caldera dynamical behaviour. Geophys. J. Int. 105, 365–379.

Clauser, C., Huenges, E., 1995. Thermal conductivity of rocks and minerals. In: Ahrens, T.J. (Ed.), Rock Physics and Phase

Relations, a Handbook of Physical Constant. Amr. Geophys. Union Ref. Shelf, vol. 3. AGU, Washington DC, pp. 105–126.

Corrado, G., De Lorenzo, S., Mongelli, F., Tramacere, A., Zito, G., 1998. Surface heat flow density at the Phlegrean Field Caldera (southern Italy). Geothermics 27, 469–484.

Criss, R.E., Fleck, R.J., Taylor Jr, H.P., 1991. Tertiary meteoric hydrothermal systems and their relation to ore deposition, Northwestern United States and Southern British Columbia. J. Geophys. Res. 96, 13335–13356.

Cundall, P.A., 1989. Numerical experiments on localization in frictional materials. Ingenieur-Archiv. 59, 148–159.

Cundall, P.A., Board, B., 1988. A microcomputer program for modeling large-strain plasticity problems. Proc. Sixth International Conference on Numerical Methods in Geomechanics. Balkema, Rotterdam, pp. 2101–2108.

Cunningham, C.G., Steven, T.A., 1979. Mount Belknap and Red Hills Calderas and associated rocks, Marysvale volcanic field, west-central Utah. U.S. Geol. Surv. Bull. 1468, 1–34.

Cunningham, C.G., Arribas Jr, A., Rytuba, J.J., Arribas, A., 1990. Mineralized and unmineralized calderas in Spain; Part I, evolution of the Los Frailes caldera. Miner. Deposita 25, S21–S28.

Cunningham, C.G., Aparicio, H.N., McKee, E.H., Ericksen, G.E., Tavera, F.V., 1994. Relationship between the Porco, Bolivia, Ag–Zn–Pb–Sn deposit and the Porco caldera. Econ. Geol. 89, 1833–1841.

De Natale, G., Petrazzuoli, S.M., Pinque, F., 1997. The effect of collapse structures on ground deformations in calderas. Geophys. Res. Lett. 24, 1555–1558.

England, P.C., Richardson, S.W., 1980. Erosion and age dependence of continental heat flow. Geophys. J. R. Astron. Soc. 62, 421–437.

Garfunkel, Z., Anderson, C.A., Shubert, G., 1986. Mantle circulation and the lateral migration of subducted slabs. J. Geophys. Res. 91, 7205–7223.

Gazis, C.A., Lanphere, M., Taylor Jr, H.P., Gurbanov, A., 1995. $^{40}Ar/^{39}Ar$ and $^{18}O/^{16}O$ studies of the Chegem ash-flow caldera and the Eldjurta granite: cooling of two Late Pliocene igneous bodies in the Greater Caucasus mountains, Russia. Earth Planet. Sci. Lett. 134, 377–391.

Gerbault, M., Poliakov, A.N.B., Daignieres, M., 1998. Prediction of faulting from the theories of elasticity and plasticity: what are the limits?. J. Struct. Geol. 20, 301–320.

Goff, F., Gardner, J.N., 1994. Evolution of a mineralized geothermal system, Valles caldera, New Mexico. Econ. Geol. 89, 1803–1832.

Gray, J.E., Coolbaugh, M.F., 1994. Geology and Geochemistry of Summitville, Colorado: an epithermal acid sulfate deposit in a volcanic dome. Econ. Geol. 89, 1906–1923.

Gudmunsson, A., 1998. Formation and development of normal-fault calderas and the initiation of large explosive eruptions. Bull. Volcanol. 60, 160–170.

Guillou-Frottier, L., Buttles, J., Olson, P., 1995. Laboratory experiments on the structure of subducted lithosphere. Earth Planet. Sci. Lett. 133, 19–34.

Hedenquist, J.W., Lowenstern, J.B., 1994. The role of magmas in the formation of hydrothermal ore deposits. Nature 370, 519–527.

Hill, D.P., Sorey, M.L., Ellsworth, W.L., Sass, J., 1998. Scientific drilling continues in Long Valley Caldera, California. Eos Trans. AGU 79, 429.

Jannas, R.R., Beane, R.E., Ahler, B.A., Brosnahan, D.R., 1990. Gold and copper mineralization at the El Indio deposit, Chile. J. Geochem. Explor. 36, 233–266.

Jones, R.H., Stewart, R.C., 1997. A method for determining significant structures in a cloud of earthquakes. J. Geophys. Res. 102, 8245–8254.

Karpov, G.A., Naboko, S.I., 1990. Metal contents of recent thermal waters, mineral precipitates and hydrothermal alteration in active geothermal fields, Kamchatka. J. Geochem. Explor. 36, 57–71.

Kirby, S.H., Kronenberg, A.K., 1987. Rheology of the lithosphere: selected topics. Rev. Geophys. 25, 1219–1244.

Lipman, P.W., 1984. The roots of ash-flow calderas in Western North America: windows into the top of granitic batholiths. J. Geophys. Res. 89, 8801–8841.

Lipman, P.W., 1992. Ash-flow calderas as structural controls of ore deposits - recent work and future problems. U.S. Geol. Soc. Bull., L1–L12.

Lipman, P.W., 1997. Subsidence of ash-flow calderas: relation to caldera size and magma-chamber geometry. Bull. Volcanol. 59, 198–218.

Lipman, P.W., Sawyer, D.A., 1985. Mesozoic ash-flow caldera fragments in southeastern Arizona and their relation to porphyry copper deposits. Geology 13, 652–656.

Lipman, P.W., Bogatikov, O.A., Tsvetkov, A.A., Gazis, C., Gurbanov, A.G., Hon, K., Koronovsky, N.V., Kovalenko, V.I., Marchev, P., 1993. 2.8-Ma ash-flow caldera at Chegem River in the northern Caucasus mountains (Russia), contemporaneous granites, and associated ore deposits. J. Volcanol. Geotherm. Res. 57, 85–124.

Llosa, F., Lescuyer, J.-L., Milési, J.-P., 1996. Minas Conga: Descubrimiento, Exploracion y Marco Geologico de los Porfidos Au–Cu en la Region de Cajamarca. Proc. Second International Gold Symposium, Peru, pp. 275–283.

Marcoux, E., Milési, J.-P., Sitorus, T., Simandjuntak, M., 1996. The epithermal Au–Ag–(Mn) deposit of Pongkor (West Java, Indonesia). Indonesian Mining J. 2, 1–17.

Marti, J., Ablay, G.J., Redshaw, L.T., Sparks, R.S.J., 1994. Experimental studies of collapse calderas. J. Geol. Soc. London 151, 919–929.

McKee, E.H., 1979. Ash-flow sheets and calderas: their genetic relationship to ore deposits in Nevada. Geol. Soc. Am. Spec. Pap. 180, 205–211.

Milési, J.-P., Marcoux, E., Nehlig, P., Sunarya, Y., Sukandar, A., Felenc, J., 1994. Cirotan, West Java, Indonesia: a 1.7 Ma hybrid epithermal Au–Ag–Sn–W deposit. Econ. Geol. 89, 227–245.

Milési, J.-P., Marcoux, E., Sitorus, T., Simandjuntak, M., Leroy, J., Bailly, L., 1999. Pongkor (West Java, Indonesia): a Pliocene supergene-enriched epithermal Au–Ag–(Mn) deposit. Miner. Deposita 34, 131–149.

Mitchell, A.H.G., 1996. Distribution and genesis of some epizonal Zn–Pb and Au provinces in the Carpathian–Balkan region. Trans. Instn Min. Metall. (Sect. B. Appl. Earth Sci.) 105, B127–B138.

Mitchell, A.H.G., Balce, G.R., 1990. Geological features of some epithermal gold systems, Philippines. J. Geochem. Explor. 35, 241–296.

Noble, D.C., McKee, E.H., 1982. Nevado Portugueza volcanic center, central Peru: a Pliocene central volcano-collapse caldera complex with associated silver mineralization. Econ. Geol. 77, 1893–1900.

Petersen, U., Noble, D.C., Arenas, M.J., Goodell, P.C., 1977. Geology of the Julcani mining district, Peru. Econ. Geol. 72, 931–949.

Poliakov, A.N.B.,, Cundall, P., Podlachikov, Y., Laykhovsky, V., 1993. An explicit inertial method for the simulation of visco-elastic flow: an evaluation of elastic effects on diapiric flow in two- and three-layers models. In: Stone, D.B., Runcorn, S.K. (Eds.), Flow and Creep in the Solar System: Observations, Modeling and Theory, Dynamic Modeling and Flow in the Earth and Planets. Kluwer, Holland, pp. 175–195.

Ratté, J.C., Marvin, R.F., Naeser, C.W., Bikerman, M., 1984. Calderas and ash-flow tuffs of the Mogollon Mountains, Southwestern New Mexico. J. Geophys. Res. 89, 8713–8732.

Redwood, S.D., 1987. The Soledad caldera, Bolivia: a Miocene caldera with associated epithermal Au–Ag–Cu–Pb–Zn mineralization. Geol. Soc. Am. Bull. 99, 395–404.

Roche, O., Druitt, T.H., Merle, O., 2000. Experimental study of caldera formation. J. Geophys. Res. 105, 395–416.

Ryan, M.P., 1987. Neutral buoyancy and the mechanical evolution of magmatic systems. In: Mysen, B.O. (Ed.), Magmatic Processes: Physicochemical principles. Geochem. Soc. Spec. Pub., vol. 1, pp. 259–287.

Rytuba, J.J., 1994. Evolution of volcanic and tectonic features in caldera settings and their importance in the localization of ore deposits. Econ. Geol. 89, 1687–1696.

Rytuba, J.J., Arribas Jr, A., Cunningham, C.G., McKee, E.H., Podwysocki, M.H., Smith, J.G., Kelly, W.C., Arribas, A., 1990. Mineralized and unmineralized calderas in Spain; part II, evolution of the Rodalquilar caldera complex and associated gold-alunite deposits. Miner. Deposita 25, S29–S35.

Sander, M.V., Einaudi, M.T., 1990. Epithermal deposition of gold during transition from propylitic to potassic alteration at Round Mountain, Nevada. Econ. Geol. 85, 285–311.

Seki, Y., 1993. Geologic setting of the Takatama gold deposit, Japan: an example of caldera-related epithermal gold mineralization. Resource Geol. Spec. Issue 14, 123–136.

Semple, D.G., Corbett, G.J., Leach, T.M., 1998. Tokuluma gold–silver deposit. In: Berkman, D.A., McKenzie, D.H. (Eds.), Geology of Australian and Papua New Guinea: Mineral Deposits. The Australian Institute of Mining and Metallurgy, Melbourne, pp. 837–842.

Sibson, R.H., 1987. Earthquake rupturing as a mineralizing agent in hydrothermal systems. Geology 15, 701–704.

Sillitoe, R.H., 1989. Gold deposits in western Pacific island arcs: the magmatic connection. Econ. Geol. Monograph 6, 274–291.

Sillitoe, R.H., 1994. Erosion and collapse of volcanoes: cause of telescoping in intrusion-centered ore deposits. Geology 22, 945–948.

Slack, J.F., 1980. Multistage vein ores of the Lake City District, Western San Juan Mountains, Colorado. Econ. Geol. 75, 963–991.

Smith, R.L., Bailey, R.A., 1968. Resurgent cauldrons. Geol. Soc. Am. Mem. 116, 83–104.

Sorey, M.L., Suemnicht, G.A., Sturchio, N.C., Nordquist, G.A., 1991. New evidence on the hydrothermal system in Long Valley caldera, California, from wells, fluid sampling, electrical geophysics, and age determinations of hot spring deposits. J. Volcanol. Geotherm. Res. 48, 229–263.

Tsenn, M.C., Carter, N.L., 1987. Upper limits of power law creep of rocks. Tectonophysics 136, 1–26.

White, N.C., Hedenquist, J.W., 1990. Epithermal environments and styles of mineralization: variations and their causes, and guidelines for exploration. J. Geochem. Explor. 36, 445–474.

Watanabe, T., Koyaguchi, T., Seno, T., 1999. Tectonic stress controls on ascent and emplacement of magmas. J. Volcanol. Geotherm. Res. 91, 65–78.

Williams, H., 1941. Calderas and their origin. Univ. California Publ. Depart. Geol. Sci. 25, 239–346.